

Letter

# ALMA [C I] observations toward the central region of Seyfert galaxy NGC 613

Yusuke MIYAMOTO,<sup>1,\*</sup> Masumichi SETA,<sup>2</sup> Naomasa NAKAI,<sup>3,4</sup>  
Yoshimasa WATANABE,<sup>3,4</sup> Dragan SALAK,<sup>2</sup> and Shun ISHII<sup>5,6</sup>

<sup>1</sup>Nobeyama Radio Observatory, NAOJ, Nobeyama, Minamimaki, Minamisaku, Nagano 384-1305, Japan

<sup>2</sup>Department of Physics, School of Science and Technology, Kwansei Gakuin University, 2-1 Gakuen, Sanda, Hyogo 669-1337, Japan

<sup>3</sup>Division of Physics, Faculty of Pure and Applied Sciences, University of Tsukuba, Tsukuba, Ibaraki 305-8571, Japan

<sup>4</sup>Tomonaga Center for the History of the Universe, University of Tsukuba, Tsukuba, Ibaraki 305-8571, Japan

<sup>5</sup>Chile Observatory, NAOJ, 2-21-1 Osawa, Mitaka, Tokyo 181-8588, Japan

<sup>6</sup>Joint ALMA Observatory (JAO), Alonso de Córdova 3107, Vitacura 763-0355, Santiago, Chile

\*E-mail: [miyamoto.yusuke@nao.ac.jp](mailto:miyamoto.yusuke@nao.ac.jp)

Received 2017 November 21; Accepted 2018 February 1

## Abstract

We report ALMA observations of [C I] ( $^3P_1 - ^3P_0$ ),  $^{13}\text{CO}$ , and  $\text{C}^{18}\text{O}$  ( $J = 1-0$ ) toward the central region of a nearby Seyfert galaxy NGC 613. The very high resolutions of  $0''.26 \times 0''.23$  ( $=22 \times 20$  pc) for [C I] and  $0''.42 \times 0''.35$  ( $=36 \times 30$  pc) for  $^{13}\text{CO}$ , and  $\text{C}^{18}\text{O}$  resolve the circumnuclear disk (CND) and star-forming ring. The distribution of [C I] in the ring resembles that of the CO emission, although [C I] is prominent in the CND. This can be caused by the low intensities of the CO isotopes due to the low optical depths under the high temperature in the CND. We found that the intensity ratios of [C I] to  $^{12}\text{CO}(3-2)$  ( $R_{\text{C I}/\text{CO}}$ ) and to  $^{13}\text{CO}(1-0)$  ( $R_{\text{C I}/^{13}\text{CO}}$ ) are high at several positions around the edge of the ring. The spectral profiles of CO lines mostly correspond each other in the spots of the ring and high  $R_{\text{C I}/\text{CO}}$ , but those of [C I] at spots of high  $R_{\text{C I}/\text{CO}}$  are different from those of CO. These results indicate that [C I] at the high  $R_{\text{C I}/\text{CO}}$  traces different gas from that traced by the CO lines. The [C I] kinematics along the minor axis of NGC 613 could be interpreted as a bubbly molecular outflow. The outflow rate of molecular gas is higher than star formation rate in the CND. The flow could be mainly boosted by the active galactic nucleus through its radio jets.

**Key words:** galaxies: active — galaxies: individual (NGC 613) — galaxies: ISM — ISM: jets and outflows — radio lines: ISM

## 1 Introduction

Molecular hydrogen ( $\text{H}_2$ ) is a major component of the interstellar medium in galaxies. While the  $^{12}\text{CO}(J = 1-0)$  line

has been used as a principal probe in tracing molecular gas and in studying dynamics and molecular gas distribution in galaxies, it is not easy to estimate the gas mass using  $^{12}\text{CO}$

due to the large optical depth. Recently, atomic carbon (C I) has attracted attention as a good tracer of the mass of the cold molecular gas, especially in high-redshift galaxies or metal-poor objects (e.g., Papadopoulos & Greve 2004; Papadopoulos et al. 2004).

It has been recognized that C I exists predominantly in the thin layer near the surface of molecular clouds exposed to UV radiation, which is called the photodissociation region (PDR; Tielens & Hollenbach 1985; Hollenbach et al. 1991). However, large-scale C I ( $^3P_1 - ^3P_0$ ), hereafter simply referred as [C I], mapping of the Orion A and B molecular clouds revealed that [C I] coexists with  $^{12}\text{CO}$  and  $^{13}\text{CO}(1-0)$  and their intensities correlate with each other (Ikeda et al. 2002). Since the critical density of [C I] is similar to that of  $^{12}\text{CO}$  ( $n \approx 10^3 \text{ cm}^{-3}$ ), these findings indicate that the emission lines arise from the same volume and share similar excitation temperatures.

The global extent of the [C I] emission is similar to that of dense molecular gas traced by  $\text{C}^{18}\text{O}$ , whereas the intensities of [C I] and  $\text{C}^{18}\text{O}$  anti-correlate with each other (e.g., Maezawa et al. 1999). Oka et al. (2005) showed the distribution of the C I-to- $^{12}\text{CO}$  intensity ratio on the Galactic scale and suggested that the locations of the high-intensity ratio correspond to the upstream of spiral arms. These results indicate that [C I] abundance is high in the early stage of chemical evolution (within a timescale for conversion from C I to CO;  $\sim 10^6 \text{ yr}$ ) and [C I] traces young clouds which are just forming dense cores (Suzuki et al. 1992; Maezawa et al. 1999).

A couple of dozen observations toward nearby galaxy centers with single-dish telescopes that have linear resolution of several 100 pc have revealed that the intensity ratio of [C I] to  $^{13}\text{CO}$  in most galaxy centers exceeds unity, which is rare for the Galactic molecular clouds, and is likely related with the central activities (Israel 2005). The central outflow or shock may enhance [C I] compared with  $\text{CO}(1-0)$  (Krips et al. 2016), indicating the possibility of [C I] being an outflow or shock tracer. On the other hand, the distribution of [C I] is still unclear due to a few mapping observations with the limited spatial resolution (e.g., Gerin & Phillips 2000). For characterizing molecular clouds traced by C I, it is necessary to clarify the distributions of C I and CO lines relative to energetic activities, such as star formation and central outflow.

Molecular gas in barred galaxies can be transported toward the galactic center, because the galactic bar can effectively drain the angular momentum of the gas (Binney & Tremaine 2008, and references therein). The gas gathers at the region of nearly circular orbits ( $x_2$  orbits) and forms a nuclear ring which is the site of vigorous star formation ( $r \sim$  a few 100 pc; we refer to it as a star-forming ring). Star-forming rings are promising

reservoirs of the gas that feeds to the accretion disks in active galactic nuclei (AGNs) via the circumnuclear disk (CND;  $r \sim 1-100 \text{ pc}$ ).

The nearby galaxy NGC 613 hosts a low-luminosity AGN and prominent radio jets from the center (e.g., Goulding & Alexander 2009; Hummel & Jorsater 1992). The central CND of NGC 613 ( $r \lesssim 90 \text{ pc}$ ) contains abundant molecular gas, while the star formation rate (SFR) in the CND is lower than that in its star-forming ring ( $250 \lesssim r \lesssim 340 \text{ pc}$ ), which is probably caused by the interaction between the jets and gas in the CND (Falc3n-Barroso et al. 2014; Davies et al. 2017; Miyamoto et al. 2017). Comparisons between [C I] and CO lines in the energetic activities could provide clues to understanding what [C I] traces. This letter reports [C I] and CO observations with resolution high enough to resolve the central region of the galaxy, i.e., the CND and star-forming ring, for the first time as a galaxy.

## 2 Observations

NGC 613 was observed with the Atacama Large Millimeter/submillimeter Array (ALMA) using Band 3 and Band 8 receivers. For Band 8, the Atacama compact array (ACA) and total power array (TP) were used in addition to the 12 m array. The synthesized beams at Bands 3 and 8 were  $0''.42 \times 0''.35$  ( $\theta = -29^\circ$ ) and  $0''.26 \times 0''.23$  ( $\theta = -71^\circ$ ), corresponding to  $36 \times 30$  and  $22 \times 20 \text{ pc}$ , respectively, at the distance of the galaxy (17.5 Mpc; Tully 1988). Single-point observations and three-point mosaic observations were conducted for Band 3 and Band 8, respectively. The maximum recoverable scale for Band 3 is  $\sim 22''$ . These setups allowed us to image the CND and star-forming ring of NGC 613. The phase reference center of  $(\alpha_{\text{J2000.0}}, \delta_{\text{J2000.0}}) = (1^{\text{h}}34^{\text{m}}18^{\text{s}}.19, -29^\circ25'06''.60)$  was adopted (Miyamoto et al. 2017). The correlators for Band 3 were configured to set three spectral windows in the upper sideband to measure  $^{13}\text{CO}(1-0)$  ( $\nu_{\text{rest}} = 110.201354 \text{ GHz}$ ) and  $\text{C}^{18}\text{O}(1-0)$  ( $\nu_{\text{rest}} = 109.782176 \text{ GHz}$ ) in the 2SB dual-polarization mode. The correlators for Band 8 were configured to set one spectral window in the upper sideband to cover C I ( $^3P_1 - ^3P_0$ ) ( $\nu_{\text{rest}} = 492.160651 \text{ GHz}$ ), in the dual-polarization mode. The flux density at the Band 3 was calibrated using J2357–5311 and J0334–4008, and at Band 8 using J0006–0623 and Uranus. The time variations of amplitude and phase were calibrated using J0106–2718 and J0145–2733 for Band 3 and by J0204–1701 and J0137–2430 for Band 8.

The data were processed using the Common Astronomy Software Application (CASA; McMullin et al. 2007). The velocity resolution of each line's data obtained at different observing tracks with the 12 m array and ACA was

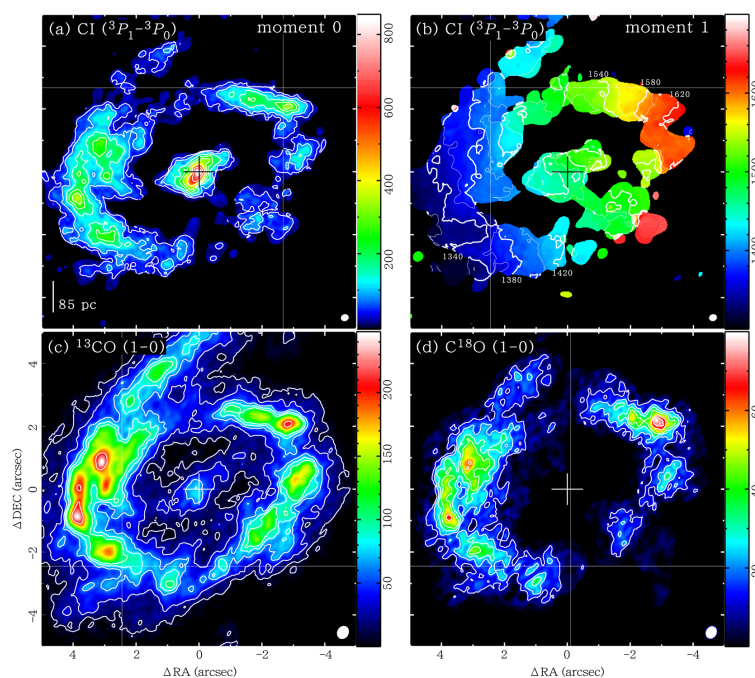


**Fig. 1.** (a) Integrated intensity map of  $\text{C I}({}^3P_1-{}^3P_0)$ . The contours are 5, 10, 20, 30, 40, 50, 60, 70, and  $80\sigma$ , where  $1\sigma = 10 \text{ K km s}^{-1}$ . (b) [C I] velocity field map derived from intensity-weighted mean velocities. The velocity is in  $\text{km s}^{-1}$  with respect to LSR and the radio definition. (c) Integrated intensity map of  ${}^{13}\text{CO}(J=1-0)$ . The contours are 5, 15, 30, 40, 50, and  $100\sigma$ , where  $1\sigma = 2 \text{ K km s}^{-1}$ . (d) Integrated intensity map of  $\text{C}^{18}\text{O}(J=1-0)$ . The contours are 5, 10, 15, 20, 35, 30, 35, 40, and  $45\sigma$  where  $1\sigma = 2 \text{ K km s}^{-1}$ . A cross in each map is the peak position of the continuum emission, i.e., the galactic center,  $(\alpha_{\text{J2000.0}}, \delta_{\text{J2000.0}}) = (1^{\text{h}}34^{\text{m}}18^{\text{s}}19, -29^{\circ}25'06''.60)$ . The filled ellipse in the bottom right-hand corner of each map represents the beam size,  $0''.26 \times 0''.23$  ( $\theta = -71^\circ$ ) for [C I] and  $0''.42 \times 0''.35$  ( $\theta = -29^\circ$ ) for  ${}^{13}\text{CO}$  and  $\text{C}^{18}\text{O}(1-0)$ .

separately rearranged to be  $10 \text{ km s}^{-1}$ . Each line's data were then combined after subtracting continuum emission determined via the channels that were free from spectral line emission. To image the continuum emission, we used the flux density at the emission-free channels. The imaging was performed using the CLEAN algorithm in CASA. CLEAN maps were obtained considering the Briggs weighting mode on the data with robustness of 0.5 for Band 3 and the natural weighting mode for Band 8. The resultant maps were  $1500 \times 1500$  pixels with  $0''.05$  per pixel and  $0''.02$  per pixel for Bands 3 and 8, respectively. For the line emission of Band 8, TP data were calibrated through flagging and the system temperature correction, and imaged independently from the 12 m array and ACA data. By using the Feather algorithm in CASA, the low-resolution image obtained via the TP and high-resolution image obtained from the 12 m array and ACA were converted into the gridded visibility plane and combined. Finally, the data was reconverted into a combined image. The sensitivities in the resultant cube of [C I],  ${}^{13}\text{CO}$ , and  $\text{C}^{18}\text{O}(J=1-0)$  are  $6 \text{ mJy beam}^{-1}$  ( $\sim 0.5 \text{ K}$ ),  $0.2 \text{ mJy beam}^{-1}$  ( $\sim 0.1 \text{ K}$ ), and  $0.2 \text{ mJy beam}^{-1}$  ( $\sim 0.1 \text{ K}$ ), respectively, in channels of  $10 \text{ km s}^{-1}$  width.

We found that the peak position of the 100 GHz continuum corresponds to the phase center with an uncertainty of  $\sim 0''.01$ , while the peak position of the 490 GHz

continuum is offset from the phase center by  $\sim 0''.07$ , which is caused by large separation of  $14''.2$  between NGC 613 and the phase calibrator (J0204–1701). We therefore shifted the position in Band 8 data so that the continuum position coincides with the center.

## 3 Results and discussion

### 3.1 Distributions of [C I] and CO lines

Figures 1a, 1c, and 1d show the integrated intensity maps of [C I],  ${}^{13}\text{CO}(J=1-0)$ , and  $\text{C}^{18}\text{O}(J=1-0)$ , respectively, where pixel values  $< 3\sigma$  in each velocity channel of the cube smoothed with twice the size of the beamwidth were masked to derive the integrated intensities of the weak emission accurately and enhance the contrasts, and figure 1b shows the intensity-weighted [C I] velocity field map. The [C I] line emission is detected both in the star-forming ring and CND, while  $\text{C}^{18}\text{O}$  is faint in the CND. The velocity field of [C I] is consistent with that of  ${}^{12}\text{CO}(3-2)$  shown by Miyamoto et al. (2017), i.e., rigid rotation in the ring. The peak positions and distribution of the [C I] emission in the ring are consistent with those of the CO emission, but are inconsistent with them in the CND. In accordance with Ikeda et al.

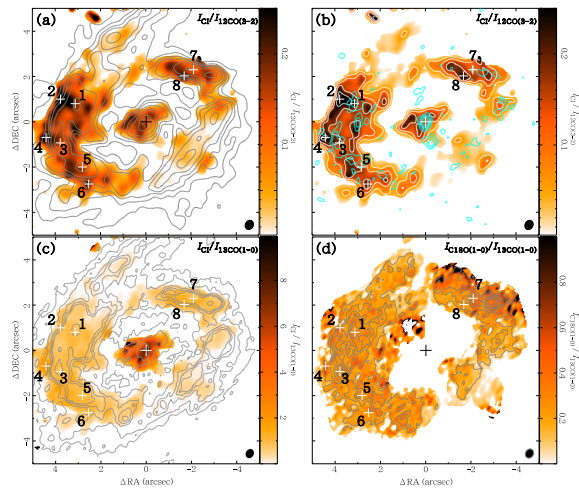


**Fig. 2.** (a) Map (color) of the integrated intensity ratio of  $I_{\text{C I}}/I_{\text{CO}(3-2)}$ , which is from Miyamoto et al. (2017), overlaid with  $I_{\text{CO}(3-2)}$  contours of 5, 10, 15, 20, 30, 50, 100, 150, and 180 $\sigma$  where  $1\sigma = 20 \text{ K km s}^{-1}$ . (b) Same as (a) but contours of the 100-GHz flux (cyan: 3, 5, 7, 9, 12, and 15 $\sigma$  where  $\sigma = 20 \mu\text{Jy beam}^{-1}$ ). (c) Map (color) of the integrated intensity ratio of  $I_{\text{C I}}/I_{\text{13CO}(1-0)}$ , overlaid with  $I_{\text{13CO}(1-0)}$  contours (same as figure 1c). (d) Map (color) of the integrated intensity ratio of  $I_{\text{C}^{18}\text{O}(1-0)}/I_{\text{13CO}(1-0)}$ , overlaid with  $I_{\text{13CO}(1-0)}$  contours (same as figure 1d).

(2002), we calculated the optical depths of [C I],  $^{13}\text{CO}(1-0)$ , and  $\text{C}^{18}\text{O}(1-0)$  under a local thermodynamic equilibrium (LTE) assumption, where those excitation temperatures are similar, and we adopted the rotational temperatures of  $T_{\text{rot}} \sim 18 \text{ K}$  in the CNB and  $T_{\text{rot}} \sim 12 \text{ K}$  in the ring as the excitation temperatures (Miyamoto et al. 2017). The optical depths of [C I] in the CNB and in the ring are estimated to be  $\tau_{\text{C I}} = 0.6 \pm 0.3$  and  $\sim 0.1-1.5$ , respectively, and those of  $^{13}\text{CO}(1-0)$  and  $\text{C}^{18}\text{O}(1-0)$  are thin in both the CNB and ring;  $\tau_{\text{13CO}} = 0.06 \pm 0.01$  (CNB) and  $\sim 0.1-0.4$  (ring), and  $\tau_{\text{C}^{18}\text{O}} \sim 0.02 \pm 0.01$  (CNB) and  $\sim 0.02-0.08$  (ring). The relatively high optical depth of [C I] in the ring can be caused by the underestimation of the excitation temperature. The corresponding distributions of [C I] and  $^{13}\text{CO}(1-0)$  in the ring are consistent with the previous studies about the Galactic components (e.g., Shimajiri et al. 2013), indicating a clumpy PDR model, in which UV radiation can penetrate deeper in a clumpy cloud (Spaans 1996), and/or a chemical evolution model (e.g., Oka et al. 2001; Ikeda et al. 2002).

Figures 2a and 2c show the integrated line ratios of [C I] to  $^{12}\text{CO}(3-2)$  ( $\equiv R_{\text{C I}/\text{CO}}$ ) and [C I] to  $^{13}\text{CO}(1-0)$  ( $\equiv R_{\text{C I}/\text{13CO}}$ ), where the  $^{12}\text{CO}$  intensity map is from Miyamoto et al. (2017) and the beam size of [C I] is convolved with those of the CO. For comparison, the distribution of the 100 GHz continuum, the flux density of which can be dominated by free-free thermal emission from H II regions followed by non-thermal emission, such as radio jets (e.g., Condon 1992; Salak et al. 2017), is superposed on the ratio map of  $R_{\text{C I}/\text{CO}}$  in figure 2b.  $R_{\text{C I}/\text{CO}}$  is in the range of 0.1–0.3 in both

the CNB and star-forming ring, and high at several spots on the edge of the ring. The temperature ratio of [C I] to CO at the spots,  $T_{\text{C I}}/T_{\text{CO}} \sim 0.6$ , is enhanced to more than double that in the ring,  $\sim 0.1-0.3$  (see channel map in supplementary material). The high  $R_{\text{C I}/\text{CO}}$  is likely located around the bright spots in the 100 GHz continuum, although not always as in the southwest region. The  $R_{\text{C I}/\text{13CO}}$  is strikingly very high in the CNB due to the low intensity of  $^{13}\text{CO}$ , although it is high at the edge of the ring, as is the case in  $R_{\text{C I}/\text{CO}}$ . The low intensity of  $^{13}\text{CO}$  relative to  $^{12}\text{CO}$  (and C I) in the CNB can be due to the low optical depth, not the extreme abundance of  $^{13}\text{CO}$ , which is caused by selective photo-dissociation, fractionation, or nucleosynthesis (e.g., Langer et al. 1984; van Dishoeck & Black 1988; Casoli et al. 1992). The selective photo-dissociation and nucleosynthesis are inconsistent with the lower rate of star formation activity in the CNB than in the ring (Falc3n-Barroso et al. 2014). In addition, the lower intensity ratio of  $\text{C}^{18}\text{O}$  to  $^{13}\text{CO}$  in the CNB than in the ring (figure 2d) cannot be explained by the fractionation, since the high temperature in the CNB (e.g.,  $T_{\text{k}} = 350-550 \text{ K}$ ; Miyamoto et al. 2017) makes the formation of  $^{13}\text{CO}$  ineffective, in contrast to  $\text{C}^{18}\text{O}$  which does not undergo the fractionation. We found that an  $R_{\text{C I}/\text{13CO}}$  of  $\sim 10$  in the CNB is consistent with the ratio of the optical depths of  $\tau_{\text{C I}} = 0.6 \pm 0.3$  to  $\tau_{\text{13CO}} = 0.06 \pm 0.01$ . In addition, it is expected that the low optical depth and high temperature in the CNB cause the ratio of the fractions of the upper state level of  $^{13}\text{CO}$  (and  $\text{C}^{18}\text{O}$ ) to the  $J = 1$  level. In NGC 1068, a case in which the intensities of CO isotopic species of the  $J = 1-0$  transition in the CNB were lower than the intensities in the ring and of the higher transition  $J = 3-2$  in the CNB was reported (Takano et al. 2014; Nakajima et al. 2015).

Figure 3 shows the spectra of [C I],  $^{12}\text{CO}(3-2)$ ,  $^{13}\text{CO}(1-0)$ , and  $\text{C}^{18}\text{O}(1-0)$  at representative positions on the CNB and ring. Spots 1, 3, 5, and 7 are peaks on the ring traced by  $\text{CO}(3-2)$  and  $^{13}\text{CO}(1-0)$  (see figures 2a and 2c), whereas spots 2, 4, 6, and 8 show the high intensity ratio of  $R_{\text{C I}/\text{CO}}$  at the edge of the ring. The profiles of the CO lines mostly correspond to each other at all spots, but those of C I at spots of high  $R_{\text{C I}/\text{CO}}$  have different velocity features from those of CO. The different spectral profiles at the high  $R_{\text{C I}/\text{CO}}$  suggest that C I traces different gas from that traced by the CO lines. In the high  $R_{\text{C I}/\text{CO}}$  at the edge of the ring, [C I] would trace dark CO, e.g., an early stage of chemical evolution (Tanaka et al. 2011), although other models, including the PDR model, cannot be excluded. In order to clarify the reason for the different spectral profiles, multi-wavelength observations with angular resolution high enough to resolve individual molecular clouds ( $\lesssim 10 \text{ pc}$ ) are needed, since PDR models are developed to represent the structure of an individual cloud.

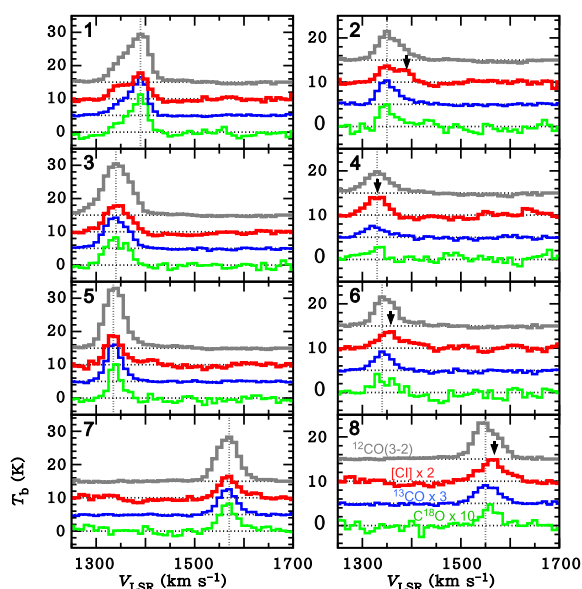


Fig. 3. Spectra of [C I], CO(3–2),  $^{13}\text{CO}(1-0)$  and  $\text{C}^{18}\text{O}(1-0)$  at the spots denoted in figure 2. The corresponding aperture is  $0''.5$  (42 pc).

### 3.2 [C I] outflow in a circumnuclear disk (CND)

Figure 4b shows the position–velocity (PV) diagram of [C I] of NGC 613 along the minor axis with  $PA = 28^\circ$  (figure 4a), superposed on the PV diagram of CO(3–2). The gas motion in NGC 613 is counterclockwise and the southern part of NGC 613 is on the near side (figure 1b; Burbidge et al. 1964). In the southern region ( $Y \sim -1''.0$ ), we found some compact components (A, B, and C) of size  $\sim 0''.4$  ( $= 34$  pc) and velocity width of  $\sim 10 \text{ km s}^{-1}$ , consistent with those of giant molecular cloud (e.g., Sanders et al. 1985). Especially, the location of component B at  $Y \sim -1''.0$  ( $= 85$  pc) is close to the peak of the southern

bubble traced by the 4.9-GHz continuum, the flux density of which is dominated by synchrotron emission due to the nuclear jets (Hummel & Jorsater 1992). The [C I] intensities of 15.7, 44.0, and  $14.7 \text{ K km s}^{-1}$  of components A, B, and C correspond to the column densities of  $N_{\text{C I}} = 2.7, 7.6, \text{ and } 2.5 \times 10^{17} \text{ cm}^{-2}$ , respectively, according to Ikeda et al. (2002) and  $\tau_{\text{C I}} \sim 0.6$  in the CND. The ratio of  $N(\text{C I})$  to  $N(\text{CO})$  in the ring becomes  $\sim 0.1$ , where we adopted  $N(\text{CO}) = 7.0 \times 10^{16} \int T_{\text{b}}(^{13}\text{CO}) dv \tau_{^{13}\text{CO}} / [1 - \exp(-\tau_{^{13}\text{CO}})] [\text{cm}^{-2}]$  by assuming  $T_{\text{ex}}(\text{ring}) \sim 12 \text{ K}$  and  $[^{12}\text{CO}]/[^{13}\text{CO}] = 60$  (cf. Ikeda et al. 2002). We estimated total (atomic and molecular) gas masses of components A, B, and C to be roughly  $8.2, 63.0, \text{ and } 3.6 \times 10^4 M_{\odot}$ , respectively, adopting a relation of total hydrogen carbon column density to that of carbon,  $N_{\text{H}} \approx 2500[N(\text{CO}) + N(\text{C})]$  (Israel & Baas 2001, 2003 and references therein), although these values can be underestimated since column density of the ionized carbon is not accounted here.

The gas components may expand spherically because of the symmetric velocity patterns of the components and the edge relative to  $V_{\text{sys}}$  in figure 4b. We assumed that the velocity difference between the edge and  $V_{\text{sys}}$  is the same as the expanding velocities of all components,  $v_{\text{exp}} \sim 35[(1510 - 1440)/2]/(\cos i_{\text{out}}) \text{ km s}^{-1}$ , where  $i_{\text{out}}$  is an angle between a normal line to the bubble and the line of sight. The offset between the averaged velocity of the edge and  $V_{\text{sys}}$  could be caused by an inclination of the outflow to the line-of-sight, although the velocity resolution  $\Delta V = 10 \text{ km s}^{-1}$  is not good enough to permit further discussion. Taking the height of the component B to be  $\sim 85$  pc and the expanding velocity of  $v_{\text{exp}} \sim 35 \text{ km s}^{-1}$  as a lower limit, the expanding time is  $t_{\text{exp}} \sim 2.4 \text{ Myr}$ , and the mass outflow rate of only component B becomes  $dM_{\text{H}_2}/dt \sim 0.3 M_{\odot} \text{ yr}^{-1}$ , which is

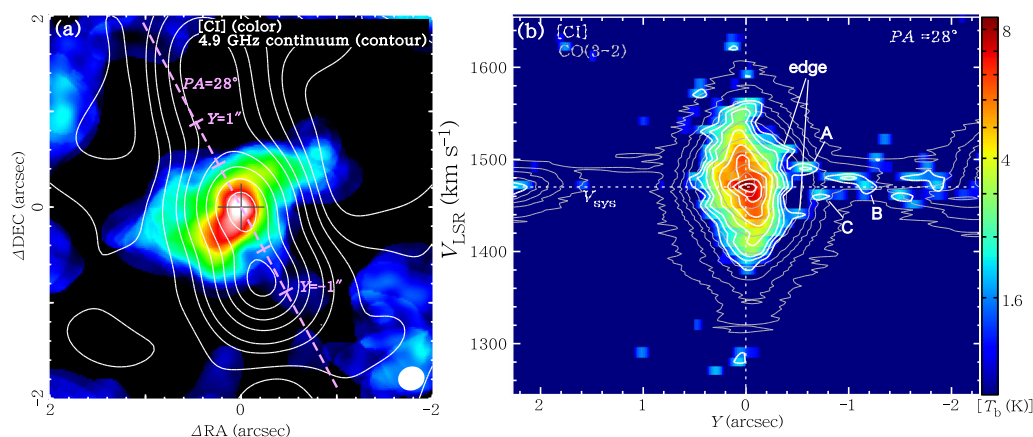


Fig. 4. (a) Enlarged view of the integrated intensity maps of [C I] in figure 1a (color) is overlaid with the 4.9-GHz continuum from Miyamoto et al. (2017) (contours). (b) Position–velocity (PV) diagram of [C I] along the minor axis of NGC 613;  $PA = 28^\circ$  (Miyamoto et al. 2017) (Color image and white contours). The levels of the contours are 3, 4, 5, 7, 9, 11, 13, 15, and  $17\sigma$  where  $\sigma = 0.5 \text{ K}$ . Gray contours show the PV diagram of CO(3–2) from Miyamoto et al. (2017), and the levels are 5, 15, 20, 30, 50, 70, 90, and  $100\sigma$  where  $\sigma = 0.25 \text{ K}$ .

higher than the SFR in the CNB,  $0.02 M_{\odot} \text{yr}^{-1}$  (Falcón-Barroso et al. 2014). It is noted that the mass outflow rate of nearby starburst galaxies, e.g., M82 (Salak et al. 2013), NGC 253 (Bolatto et al. 2013), and NGC 1808 (Salak et al. 2016), is comparable to the SFR. The AGN bolometric luminosity of NGC 613 is a few  $10^{42} \text{erg s}^{-1}$ , accounting for  $\sim 10\%$  of total luminosity, including a contribution from shock excitation and star formation (Davies et al. 2017). In addition, the Eddington luminosity is  $L_{\text{edd}} = 1.3 \times 10^{45} \text{erg s}^{-1}$ , found by adopting an expected black hole mass of  $\sim 10^7 M_{\odot}$  (Beifiori et al. 2012). The kinetic energy and luminosity of the outflowing component become  $1/2 M_{\text{H}_2} v_{\text{exp}}^2 \sim 7.7 \times 10^{51} \text{erg}$  and  $1/2 dM_{\text{H}_2}/dt v_{\text{exp}}^2 \sim 1.0 \times 10^{38} \text{erg s}^{-1}$ , respectively. The jet power  $P_{\text{jet}} = 1.5 \times 10^{42} \text{erg s}^{-1}$ , which can be estimated by adopting the central 1.4-GHz luminosity of  $3.98 \times 10^{37} \text{W Hz}^{-1}$  (Hummel et al. 1985) to a scaling relation suggested by Cavagnolo et al. (2010), is larger than the kinetic luminosity. The ratio of  $P_{\text{jet}}/L_{\text{edd}} = 1.2 \times 10^{-3}$  is consistent with a value expected from a numerical simulation, within the range of which the jet can drive the interstellar medium efficiently (Wagner et al. 2012). These results indicate that the jet contributes towards driving the gas outflow, although the [C I] outflow is tentative. In order to confirm the outflow, more sensitive [C I] observations are needed.

## Acknowledgments

We are grateful to the anonymous referee for insightful comments that improved this paper. This paper makes use of the following ALMA data: ADS/JAO. ALMA#2015.1.01487.S. ALMA is a partnership of ESO (representing its member states), NSF (USA) and NINS (Japan), together with NRC (Canada) and NSC and ASIAA (Taiwan) and KASI (Republic of Korea), in cooperation with the Republic of Chile. The Joint ALMA Observatory is operated by ESO, AUI/NRAO and NAOJ. This work was financially supported by Grants-in-Aid for Scientific Research (KAKENHI) of the Japanese society for the Promotion of Science (JSPS, Grant No. 16H03961).

## Supplementary data

Supplementary data are available at [PASJ](https://doi.org/10.1093/pasj/psy016/4964789) online.

CI\_to\_co.cube\_2ch.ratio.eps

## References

- Beifiori, A., Courteau, S., Corsini, E. M., & Zhu, Y. 2012, *MNRAS*, 419, 2497
- Binney, J., & Tremaine, S. 2008, *Galactic Dynamics*, 2nd ed. (Princeton: Princeton University Press)
- Bolatto, A. D., et al. 2013, *Nature*, 499, 450
- Burbidge, E. M., Burbidge, G. R., Rubin, V. C., & Prendergast, K. H. 1964, *ApJ*, 140, 85
- Casoli, F., Dupraz, C., & Combes, F. 1992, *A&A*, 264, 55
- Cavagnolo, K. W., McNamara, B. R., Nulsen, P. E. J., Carilli, C. L., Jones, C., & Birzan, L. 2010, *ApJ*, 720, 1066
- Condon, J. J. 1992, *ARA&A*, 30, 575
- Davies, R. L., et al. 2017, *MNRAS*, 470, 4974
- Falcón-Barroso, J., Ramos Almeida, C., Böker, T., Schinnerer, E., Knapen, J. H., Lançon, A., & Ryder, S. 2014, *MNRAS*, 438, 329
- Gerin, M., & Phillips, T. G. 2000, *ApJ*, 537, 644
- Goulding, A. D., & Alexander, D. M. 2009, *MNRAS*, 398, 1165
- Hollenbach, D. J., Takahashi, T., & Tielens, A. G. G. M. 1991, *ApJ*, 377, 192
- Hummel, E., & Jorsater, S. 1992, *A&A*, 261, 85
- Hummel, E., Pedlar, A., Davies, R. D., & van der Hulst, J. M. 1985, *A&AS*, 60, 293
- Ikeda, M., Oka, T., Tatematsu, K., Sekimoto, Y., & Yamamoto, S. 2002, *ApJS*, 139, 467
- Israel, F. P. 2005, *Ap&SS*, 295, 171
- Israel, F. P., & Baas, F. 2001, *A&A*, 371, 433
- Israel, F. P., & Baas, F. 2003, *A&A*, 404, 495
- Krips, M., et al. 2016, *A&A*, 592, L3
- Langer, W. D., Graedel, T. E., Frerking, M. A., & Armentrout, P. B. 1984, *ApJ*, 277, 581
- McMullin, J. P., Waters, B., Schiebel, D., Young, W., & Golap, K. 2007, *ASP Conf. Ser.*, 376, 127
- Maizawa, H., et al. 1999, *ApJ*, 524, L129
- Miyamoto, Y., Nakai, N., Seta, M., Salak, D., Nagai, M., & Kaneko, H. 2017, *PASJ*, 69, 83
- Nakajima, T., et al. 2015, *PASJ*, 67, 8
- Oka, T., et al. 2001, *ApJ*, 558, 176
- Oka, T., et al. 2005, *ApJ*, 623, 889
- Papadopoulos, P. P., & Greve, T. R. 2004, *ApJ*, 615, L29
- Papadopoulos, P. P., Thi, W.-F., & Viti, S. 2004, *MNRAS*, 351, 147
- Salak, D., Nakai, N., Hatakeyama, T., & Miyamoto, Y. 2016, *ApJ*, 823, 68
- Salak, D., Nakai, N., Miyamoto, Y., Yamauchi, A., & Tsuru, T. G. 2013, *PASJ*, 65, 66
- Salak, D., Tomiyasu, Y., Nakai, N., Kuno, N., Miyamoto, Y., & Kaneko, H. 2017, *ApJ*, 849, 90
- Sanders, D. B., Scoville, N. Z., & Solomon, P. M. 1985, *ApJ*, 289, 373
- Shimajiri, Y., et al. 2013, *ApJ*, 774, L20
- Spaans, M. 1996, *A&A*, 307, 271
- Suzuki, H., Yamamoto, S., Ohishi, M., Kaifu, N., Ishikawa, S.-I., Hirahara, Y., & Takano, S. 1992, *ApJ*, 392, 551
- Takano, S., et al. 2014, *PASJ*, 66, 75
- Tanaka, K., Oka, T., Matsumura, S., Nagai, M., & Kamegai, K. 2011, *ApJ*, 743, L39
- Tielens, A. G. G. M., & Hollenbach, D. 1985, *ApJ*, 291, 747
- Tully, R. B. 1988, *Nearby Galaxies Catalog* (Cambridge: Cambridge University Press)
- van Dishoeck, E. F., & Black, J. H. 1988, *ApJ*, 334, 771
- Wagner, A. Y., Bicknell, G. V., & Umemura, M. 2012, *ApJ*, 757, 136